INORGANIC CHEMISTRY FRONTIERS

RESEARCH ARTICLE

View Article Online
View Journal | View Issue

Cite this: *Inorg. Chem. Front.*, 2025, **12**, 6803

A series of pinwheel-shaped Ln_{21}-oxo-cluster-embedded polyoxometalates as single-crystal proton-conductive and tunable photoluminescent materials†

Yun-Fei Cao, Xin-Rong Jin, Wen-Jun Xia, Yan-Qiong Sun, * Xin-Xiong Li and Shou-Tian Zheng *

The integration of high-nuclearity lanthanide-oxo (Ln-O) clusters into polyoxotungstates (POTs) presents a formidable synthetic challenge due to intricate assembly mechanisms and the labile nature of lanthanide coordination. Herein, we present an innovative alkaline-mediated templating strategy for constructing unprecedented Ln-oxo-cluster-encapsulated POTs through the synergistic assembly of lacunary polyoxotungstate precursors with *in situ* generated Ln-oxo clusters. This approach employs basic N-containing ligands and selenite (SeO_3^{2-}) anions as synergistic structure-directing agents. Guided by this approach, we have successfully synthesized two series of giant Ln_{21}-oxo-cluster-embedded polyoxotungstates, $H_{23}K_{30}(H_2O)_{18}\{[Ln_{21}(H_2O)_9(WO_6)(SeO_3)_6][Ln_3(SeO_3)_2]_2(GeW_{10}O_{38})_9\}$·solvent (**1-Ln**) (Ln = Eu, Gd, Tb, Dy) and $H_{27}Na_3K_{21}(H_2O)_{11}(MePIP)_2\{[Ln_{21}(H_2O)_9(WO_6)(SeO_3)_6][Ln_3(SeO_3)_2]_2(GeW_{10}O_{38})_9\}$·solvent (**2-Ln**) (Ln = Eu, Tb, MePIP = *N*-methylpiperazine). Notably, these compounds feature a rare pinwheel-shaped high-nuclearity Ln_{21}-oxo-cluster-embedded polyanion, $\{[Ln_{21}(H_2O)_9(WO_6)(SeO_3)_6][Ln_3(SeO_3)_2]_2(GeW_{10}O_{38})_9\}$ ($\{\mathbf{Ln_{27}Se_{10}Ge_9W_{91}}\}$), with a three-layered sandwich structure. Compounds **1-Eu** and **2-Eu** exhibit distinct proton conduction properties due to their different packing structures. In particular, **1-Eu** demonstrates a high single-crystal proton conductivity of 1.8×10^{-2} S cm^{-1} at 98% RH and 25 °C along the [001] channel direction, outperforming most crystalline porous materials. Additionally, **1-Eu** exhibits temperature-dependent fluorescence. The $\mathbf{1\text{-}Eu_{0.25}Dy_{0.75}}$ sample can emit macroscopic white light under blue irradiation. This work provides a feasible strategy for constructing high-nuclearity Ln-oxo-cluster-containing POTs and expands their application in smart proton conductive materials and multicolor luminescent systems.

Received 6th May 2025,
Accepted 19th June 2025

DOI: 10.1039/d5qi01071c

rsc.li/frontiers-inorganic

Introduction

Polyoxometalates (POMs) have emerged as exceptional proton-conductive materials owing to their structural diversity, tunable dimensions/charges, excellent redox activities, and remarkable electron and proton transfer/storage capabilities coupled with good stability.[1–15] Concurrently, lanthanide (Ln)-based compounds play an important role in the field of luminescent materials due to their distinctive 4f electronic configuration, high internal quantum efficiency, narrow f–f transition and tunable photoluminescence properties.[16–20] At the same time, POMs are anions with a large number of O atoms on the surface. The electrostatic attractions between lanthanide ions and POMs, together with the desirable hard Lewis acid/base match, make POMs an attractive class of protecting ligands and/or templating anions for the assembly of lanthanide clusters. POMs can sensitize lanthanide emission *via* the excitation of the ligand-to-metal charge transfer (LMCT) bands of the POM moieties, resulting in the intramolecular energy transfer from O → metal excited states to the excited levels of Ln^{3+}. Therefore, the assembly of Ln^{3+} and POMs together has become the main target of synthesizing new multifunctional Ln-POM materials with notable and enhanced physico-chemical features.[21,22]

Over the past decade, significant advancements have been made in the structural design and Ln-nuclearity expansion of the Ln-containing polyoxotungstates (Ln-POTs). The lacunary

Fujian Provincial Key Laboratory of Advanced Inorganic Oxygenated Materials, College of Chemistry, Fuzhou University, Fuzhou, Fujian 350108, China. E-mail: sunyq@fzu.edu.cn, stzheng@fzu.edu.cn

†Electronic supplementary information (ESI) available: Materials and methods, tables, crystal structure figures, supplementary plots including P-XRD, UV, FT-IR and Nyquist plots, emission spectra *etc*. CCDC 2387252 and 2387262. For ESI and crystallographic data in CIF or other electronic format see DOI: https://doi.org/10.1039/d5qi01071c

polyoxotungstate precursors, including $[XW_{11}]^{n-}$, $[XW_{10}]^{n-}$, and $[XW_9]^{n-}$ (X = Ge, Si, Sb, P, As, Bi), have demonstrated remarkable potential as ligands to coordinate with Ln^{3+} cations for the design and construction of novel Ln-POTs.[23–25] Despite these advances, the field of Ln-containing polyoxotungstogermanates with more than ten Ln^{3+} centers remains relatively underexplored, with only a limited number of examples reported to date. Notable examples include $\{Ln_{14}Ge_6W_{68}\}$,[26] $\{Ce_{20}Ge_{10}W_{100}\}$,[27] $\{Ce_{24}Ge_{12}W_{120}\}$,[28] $\{Ln_{27}Ge_{10}W_{106}\}$,[29] $\{Ln_{29}Ge_{10}W_{106}\}$[29] and $\{Ln_{30}Ge_{10}W_{106}\}$,[30] which feature Ln_{14}, Ln_{20}, Ln_{24}, Ln_{26}, Ln_{28} and Ln_{30} clusters, respectively. Among these, $\{Ln_{30}Ge_{10}W_{106}\}$ contains the highest nuclearity Ln_{30}-cluster reported thus far.[30] However, significant gaps remain in the syntheses of Ln-POTs, particularly those containing Ln_{21}, Ln_{22}, Ln_{23}, Ln_{25}, Ln_{27}, and Ln_{29} clusters, which have not been reported to date. Further research in this area is essential to expand the library of high-nuclearity Ln-POTs and to explore their potential applications in various fields. Traditionally, most Ln-POTs have been synthesized in acidic media using hydrothermal and volatilization methods. In these structures, Ln^{3+} ions are typically spatially separated by POT fragments rather than aggregating to form high-nuclearity Ln-O clusters. In recent years, our research has focused on developing a novel synthetic strategy to construct giant Ln-O cluster embedded Ln-POTs under alkaline conditions.[29,30] This approach involves the assembly of lacunary polyoxotungstate precursors with *in situ* generated Ln-oxo clusters in the presence of basic N-containing ligands. The N-containing organic ligands play a dual role: they form weak coordination bonds with Ln^{3+}. The weak interactions effectively prevent the rapid precipitation of Ln^{3+} in alkaline environments and facilitate the gradient release of Ln^{3+} ions through a thermally controlled slow-release mechanism. This approach not only facilitates the formation of Ln-O clusters but also offers kinetic control over cluster assembly. Additionally, the introduction of SeO_3^{2-} as an anionic template effectively blocks direct coordination pathways of metal ions,[31–34] thereby significantly increasing the likelihood of forming giant POT clusters.

Research into the properties of Ln-POTs has been largely focused on individual properties, such as photoluminescence, proton conduction, magnetism, Lewis acid–base catalysis, fluorescence probe, electrocatalysis, photochromism and ferroelectricity.[31,35–42] However, studies on bifunctional Ln-POTs, especially those with both tunable photoluminescence and proton conduction properties, remain scarce.[43,44] This highlights the need for further exploration into multifunctional Ln-POTs.

Based on the aforementioned synthetic strategy, two series of novel windmill-like Ln_{21}-oxo-cluster-embedded Ln-POTs, $H_{23}K_{30}(H_2O)_{18}\{[Ln_{21}(H_2O)_9(WO_6)(SeO_3)_6][Ln_3(SeO_3)_2]_2[(GeW_{10}O_{38})_9]\}\cdot$solvent (**1-Ln**) (Ln = Eu, Gd, Tb and Dy) and $H_{27}Na_3K_{21}(H_2O)_{11}(MePIP)_2\{[Ln_{21}(H_2O)_9(WO_6)(SeO_3)_6][Ln_3(SeO_3)_2]_2[(GeW_{10}O_{38})_9]\}\cdot$solvent (**2-Ln**) (Ln = Eu, Tb, MePIP = *N*-methylpiperazine), were successfully synthesized under alkaline conditions. Na_2SeO_3 was employed as the anionic template and *N*,*N*,*N*′,*N*′-tetramethylethylenediamine and *N*-methylpiperazine were utilized as basic ligands. Both **1-Ln** and **2-Ln** contain the $\{[Eu_{21}(H_2O)_9(WO_6)(SeO_3)_6][Eu_3(SeO_3)_2]_2[(GeW_{10}O_{38})_9]\}$ ($\{\mathbf{Eu_{27}Se_{10}Ge_9W_{91}}\}$-1 or $\{Eu_{27}Se_{10}Ge_9W_{91}\}$-2) polyanion, which represents a giant high-nuclearity Eu_{21}-oxo-cluster-embedded polyoxotungstogermanate motif with a unique three-layered sandwich structure. Notably, this giant windmill-shaped Eu_{21}-cluster is reported for the first time. The $\{\mathbf{Eu_{27}Se_{10}Ge_9W_{91}}\}$-1 or $\{Eu_{27}Se_{10}Ge_9W_{91}\}$-2 clusters are interlinked by K^+/Na^+ cations to produce a 3D inorganic POM-based framework with one-dimensional regular hexagon channels in **1-Ln** and a 2D layered structure in **2-Ln**. Compounds **1-Ln** exhibit bifunctional properties, demonstrating both high proton conductivity and temperature-dependent luminescence. Specifically, a high single-crystal proton conductivity of 1.8×10^{-2} S cm^{-1} was observed at 98% RH and 25 °C along the [001] channel direction in **1-Eu**. Furthermore, the **1-Eu$_{0.25}$Dy$_{0.75}$** sample can emit macroscopic white light under blue irradiation.

Results and discussion

Crystal structure

Single crystal X-ray diffraction analysis revealed that **1-Eu** crystallizes in the high-symmetry trigonal space group *P*-3*c*1 (Table S1†). The structure of **1-Eu** features a C_3-symmetric $\{[Eu_{21}(H_2O)_9(WO_6)(SeO_3)_6][Eu_3(SeO_3)_2]_2[(GeW_{10}O_{38})_9]\}$ cluster (denoted as $\{\mathbf{Eu_{27}Se_{10}Ge_9W_{91}}\}$**-1**, Fig. 1a), which represents a giant high-nuclearity Eu_{21}-oxo-cluster-embedded polyoxotungstogermanate cluster with a three-layered sandwich structure. The two new pinwheel-shaped clusters $\{Eu_3(SeO_3)_2(GeW_{10}O_{38})_3\}$ ($\{Eu_3Se_2(GeW_{10})_3\}$-1) serve as the top and bottom layers (Fig. 1b), while one large "Y"-shaped $\{[Eu_{21}(H_2O)_9(WO_6)(SeO_3)_6(GeW_{10}O_{38})_3]\}$($\{Eu_{21}WSe_6(GeW_{10})_3\}$-1) cluster acts as the middle layer (Fig. 1c).

The top and bottom layers are composed of C_3-symmetric $\{Eu_3Se_2(GeW_{10})_3\}$-1 fragments (Fig. 1b). Within the $\{Eu_3Se_2(GeW_{10})_3\}$-1 cluster, the three Eu atoms are interconnected through six μ_3-O atoms from two SeO_3^{2-} anions, forming a trinuclear equilateral triangular $\{Eu_3O_6\}$ ring cluster (Fig. S1a† and Fig. 1j). Each of the two SeO_3^{2-} anions coordinates with three Eu^{3+} cations, thereby generating a rare C_3-symmetric heteroatomic cage $\{Eu_3(SeO_3)_2\}$ with 11 vertices (3 Eu, 2 Se and 6 O) (Fig. S1b† and Fig. 1j). The Eu^{3+} ions in the $\{Eu_3(SeO_3)_2\}$ cluster form nine-coordinated tricapped trigonal prisms: four O atoms from two SeO_3^{2-} anions and the remaining five O atoms from the $[\alpha(1,8)\text{-}GeW_{10}O_{38}]^{12-}$ cluster. The three Eu^{3+} ions of the $\{Eu_3(SeO_3)_2\}$ cage are further encapsulated by three Keggin-type dilacunary $[\alpha(1,8)\text{-}GeW_{10}O_{38}]^{12-}$ fragments, resulting in the formation of an intriguing pinwheel-shaped $\{Eu_3Se_2(GeW_{10})_3\}$-1 cluster (Fig. S1c† and Fig. 1b). The arrangement of the three $[\alpha(1,8)\text{-}GeW_{10}O_{38}]^{12-}$ units can be represented as an equilateral triangle. The $[\alpha(1,8)\text{-}GeW_{10}O_{38}]^{12-}$ cluster units are located on each of its three vertices with a Ge···Ge distance of 10.9989 Å (Fig. 1b).

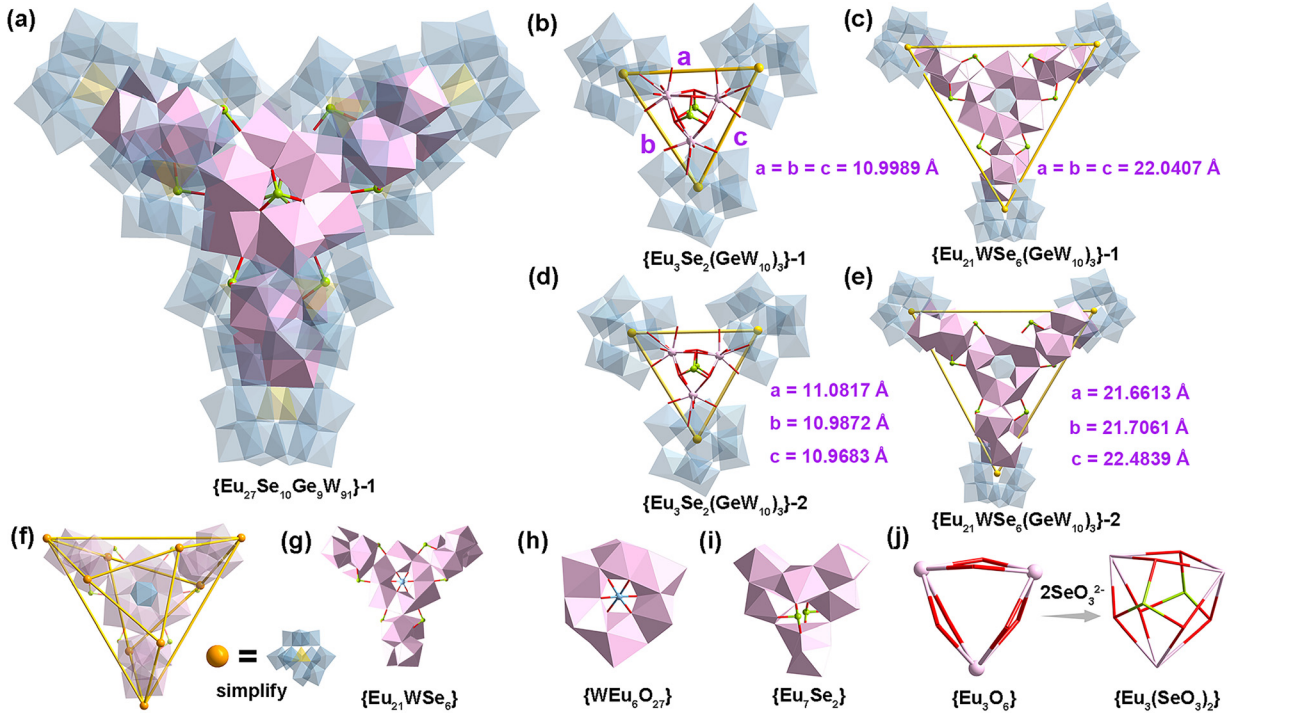

Fig. 1 (a) The structure of $\{Eu_{27}Se_{10}Ge_9W_{91}\}$-1; (b–e and g–j) views of different structural fragments in $\{Eu_{27}Se_{10}Ge_9W_{91}\}$-1 and $\{Eu_{27}Se_{10}Ge_9W_{91}\}$-2; (f) the simplified structure diagram of $\{Eu_{27}Se_{10}Ge_9W_{91}\}$-1. Color code: Se, yellow green; Ge, orange; O, red; EuO_n (n = 7, 8, 9), pink; WO_6, powder blue.

The middle layer comprises a large C_3-symmetric "Y"-shaped $\{Eu_{21}WSe_6(GeW_{10})_3\}$-1 motif, which contains a windmill-like 21-nuclearity Eu-oxo cluster $\{Eu_{21}(H_2O)_9(WO_6)(SeO_3)_6\}$ ($\{Eu_{21}WSe_6\}$) cluster and three dilacunary $[\alpha(1,8)\text{-}GeW_{10}O_{38}]^{12-}$ fragments (Fig. 1c). The C_3-symmetric $\{Eu_{21}WSe_6\}$ is comprised of three identical "T"-shaped $\{Eu_7Se_2O_{37}\}$ fragments ($\{Eu_7Se_2\}$) which serve as the windmill blades and a $\{WO_6\}$ octahedron situated at the center (Fig. S2† and 1g, 1i). In the $\{Eu_7Se_2\}$ cluster, four $\{EuO_8\}$ and one $\{EuO_9\}$ are edge or face-sharing to form a pentanuclear flattened, central tetrahedron-shaped cluster $\{Eu_5\}$ (Fig. S2a†). Two $\{EuO_7\}$ polyhedra are face-sharing to form a dinuclear $\{Eu_2O_{11}\}$ cluster (Fig. S2b†), which is linked to the $\{Eu_5O_{28}\}$ cluster by two μ_2-O oxygen atoms, resulting in a T-shaped heptanuclear Eu-oxo cluster $\{Eu_7\}$ (Fig. S2c†). The inorganic SeO_3^{2-} ligands act as linkers and anionic templates between the Eu^{3+} cations and each SeO_3^{2-} anion links three or four Eu^{3+} cations (Fig. S2d†). There are three types of coordination geometries in the $\{Eu_7\}$: two EuO_7 pentagonal bipyramids, four EuO_8 dodecahedrons, and one EuO_9 mono-capped square-antiprism (Fig. S3b† and Fig. 3c). Six SeO_3^{2-} anions and nine μ_3-O oxygen atoms link three equivalent $\{Eu_7\}$ clusters, which are related by the C_3 symmetry axis, to generate a windmill-like $\{Eu_{21}WSe_6\}$ cluster (Fig. S2f†). This cluster contains a regular hexagonal hexanuclear $\{Eu_6O_{27}\}$ ring cluster (Fig. 1h). The $\{WO_6\}$ octahedron is located at the center of the $\{Eu_6O_{27}\}$ ring cluster and is linked to six Eu^{3+} *via* six μ_3-O oxygen atoms (Fig. S2e†). The three dilacunary $[\alpha(1,8)\text{-}GeW_{10}O_{38}]^{12-}$ fragments capture three pentanuclear $\{Eu_5O_{28}\}$ clusters of $\{Eu_{21}WSe_6\}$ motif, respectively, resulting in a fascinating "Y"-shaped $\{Eu_{21}WSe_6(GeW_{10})_3\}$-1 fragment in which the three $[\alpha(1,8)\text{-}GeW_{10}O_{38}]^{12-}$ clusters comprise a large equilateral triangle with a Ge···Ge distance of 22 Å (Fig. 1c and Fig. S2†).

The two $\{Eu_3Se_2(GeW_{10})_3\}$-1 fragments are orthogonally capped above and below the "Y"-shaped $\{Eu_{21}WSe_6(GeW_{10})_3\}$-1 cluster. The $[\alpha(1,8)\text{-}GeW_{10}O_{38}]^{12-}$ clusters in the $\{Eu_3Se_2(GeW_{10})_3\}$ fragments capture the Eu^{3+} cations of $\{Eu_7Se_2\}$ cluster by W–O–Eu bonds, giving rise to a giant windwheel-shaped lanthanide-oxo-cluster-embedded sandwich polyoxotungstogermanate **$\{Eu_{27}Se_{10}Ge_9W_{91}\}$-1** cluster (Fig. 1a).

It is noteworthy that the polyanion **$\{Eu_{27}Se_{10}Ge_9W_{91}\}$-1** cluster can be described as a high-nuclearity Eu_{21}-oxo-cluster-embedded polyoxotungstogermanate, wherein the heterometal-oxo $\{Eu_{21}WSe_6\}$ nanocluster is encapsulated by nine $\{\alpha(1,8)\text{-}GeW_{10}O_{38}\}$ fragments and two $\{Eu_3(SeO_3)_2\}$ cages. The arrangement of the nine $\{\alpha(1,8)\text{-}GeW_{10}O_{38}\}$ fragments can be viewed as a distorted triangular bifrustum with nine $\{\alpha(1,8)\text{-}GeW_{10}O_{38}\}$ clusters at the vertices (Fig. 1f). The SeO_3^{2-} ions and the dilacunary $\{\alpha(1,8)\text{-}GeW_{10}O_{38}\}$ fragment play crucial roles in the formation of high-nuclearity lanthanide-oxo-cluster-containing POTs. The polyanion **$\{Eu_{27}Se_{10}Ge_9W_{91}\}$-1** clusters are interlinked by K^+ cations (K(3), K(5) and K(4)) to form a 2D (6, 3) honeycomb-like layer in the *ab* plane. These layers are further connected by $K(9)^+$ cations to produce a 3D inorganic POM-based framework with 1D regular hexagonal channels (dimensions 15.95 Å × 15.95 Å) that propagate infi-

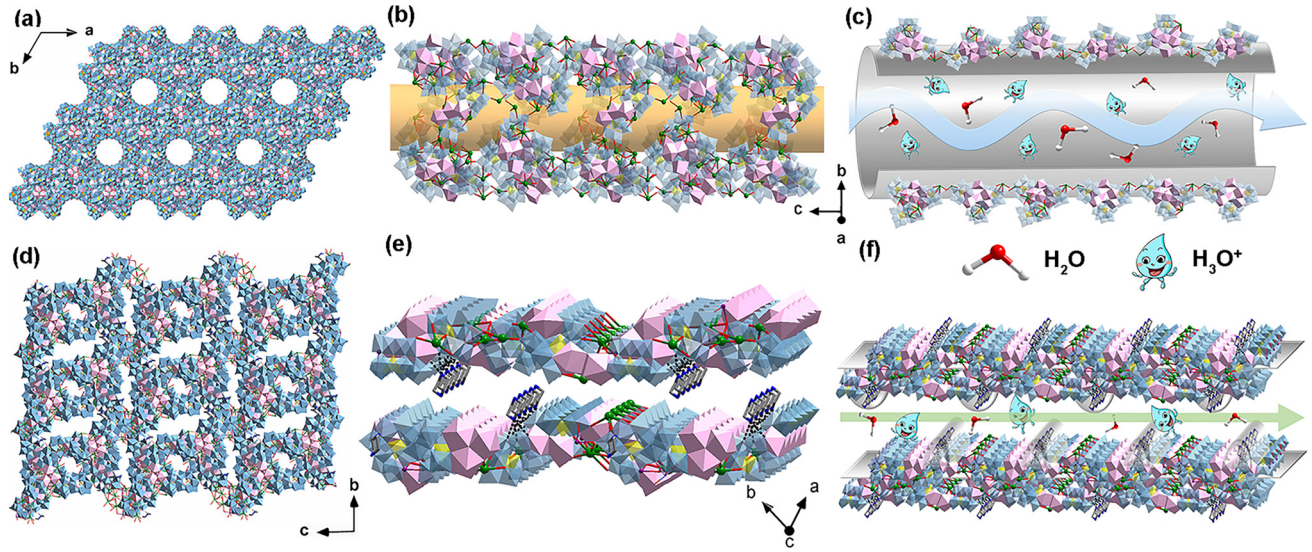

Fig. 2 (a) View of the 3D framework of **1-Eu** viewed along the *c*-axis, showing regular hexagonal channels; (b) view of a 1D nanochannel running along the *c*-axis in **1-Eu**; (c) schematic diagram of the proton transport pathway constructed using POMs, H_3O^+ and water molecules in a 1D nanochannel in **1-Eu**; (d) packing structure of the 2D layers in **2-Eu**; (e) view of the MePIP molecules intercalated between the layers in **2-Eu**; (f) schematic diagram of the proton transport pathway constructed with MePIP molecules, POMs, H_3O^+ and water molecules between the layers in **2-Eu**. Color code: Se, yellow green; Ge, orange; O, red; EuO_n (*n* = 7, 8, 9), pink; WO_6, powder blue.

nitely along the *c* axis (Fig. 2a and Fig. S3a†). This framework may promote good proton conduction. From the topological point of view, the 3D framework of **1-Eu** adopts a 5-connected *bnn* net. Each polyoxoanion **{$Eu_{27}Se_{10}Ge_9W_{91}$}-1** acts as 5-connected node, while the K^+ cations serve as linkers. The Schäfli symbol is $(4^6{\cdot}6^4)$ and the shortest closed loop around the nodes are six 4-circuits and four 6-circuits (Fig. S3b†). The *bnn* topology is rarely observed in POM-based frameworks. The coordinated water molecules point away from the POM-based framework and into the regular hexagonal channels. The guest water molecules are suspended in the channels. There are strong hydrogen bonds between the water molecules and the oxygen atoms from the polyoxoanion clusters. The hydrogen bond lengths range from 2.944(10) to 3.308(13) Å and may contribute to the proton conductivity properties.

Compound **2-Eu** crystallizes in the triclinic space group $P\bar{1}$. Its asymmetric unit comprises a gigantic POM cluster $\{[Eu_{21}O_9(WO_6)(SeO_3)_6][Eu_3(SeO_3)_2]_2[(GeW_{10}O_{38})_9]\}$ (**{$Eu_{27}Se_{10}Ge_9W_{91}$}-2**), charge-balancing 21 K^+ and 3 Na^+ counterions, as well as two *N*-methylpiperazine molecules. Despite being structurally analogous to the **{$Eu_{27}Se_{10}Ge_9W_{91}$}-1** polyoxoanion in **1-Eu**, which possesses C_3 symmetry, the polyanion **{$Eu_{27}Se_{10}Ge_9W_{91}$}-2** is devoid of such symmetry (Fig. 1d, 1e and Fig. S4†).

The key structural differences between **1-Eu** and **2-Eu** originate from two main factors: (1) counterion and organic composition: in **1-Eu**, the **{$Eu_{27}Se_{10}Ge_9W_{91}$}-1** polyoxoanion is exclusively stabilized by K^+ cations, whereas **2-Eu** incorporates a mixed counterion system including K^+, Na^+ cations and MePIP molecules; and (2) packing structures: in **1-Eu**, the K^+ cations facilitate the formation of a 3D inorganic POM-based framework with 1D regular hexagonal channels (Fig. 2a and 2b), whereas in **2-Eu**, the K^+ and Na^+ cations link the **{$Eu_{27}Se_{10}Ge_9W_{91}$}-2** polyoxoanions into a 2D layered structure, with MePIP molecules intercalated between the layers (Fig. 2d, 2e and Fig. S5†).

Compounds **1-Ln** (Ln = Eu, Gd, Tb, Dy) and **2-Ln** (Ln = Eu, Tb) were synthesized as phase-pure microcrystalline powders, exhibiting isostructural frameworks within their respective series. The structural isomorphism across two series was confirmed by comparison of their powder X-ray diffraction (PXRD) patterns and infrared (IR) spectra (Fig. S6–S9†).

Proton conduction

The presence of numerous proton hopping sites including terminal oxygen atoms of POTs, water molecules and nitrogen atoms of MePIP, as well as abundant hydrogen-bonding networks in **1-Eu** and **2-Eu**, promoted us to explore their potential applications in solid-state proton conductors (Fig. 3 and Fig. S10†). Therefore, the proton conductivity properties of **1-Eu** and **2-Eu** were investigated by alternating current (AC) impedance measurements on a compressed pellet of the crystalline powder samples. The bulk conductivity was evaluated by fitting the semicircle of the Nyquist plots.

The proton conductivities (σ) of **1-Eu** and **2-Eu** were initially evaluated at different relative humidities (RHs) (55%–98%) at 25 °C (Table S2†). The conductivity values of **1-Eu** and **2-Eu** are 1.8×10^{-3} S cm^{-1} and 2.2×10^{-4} S cm^{-1}, respectively at 55% RH. Upon increasing the RH from 55% RH to 98% RH, the conductivities increase significantly to 1.6×10^{-2} S cm^{-1} for **1-Eu** and 4.3×10^{-3} S cm^{-1} for **2-Eu** (Fig. 3a, 3d and Fig. S10a, S10c†). Notably, the conductivity of **2-Eu** increases by 20 times with the

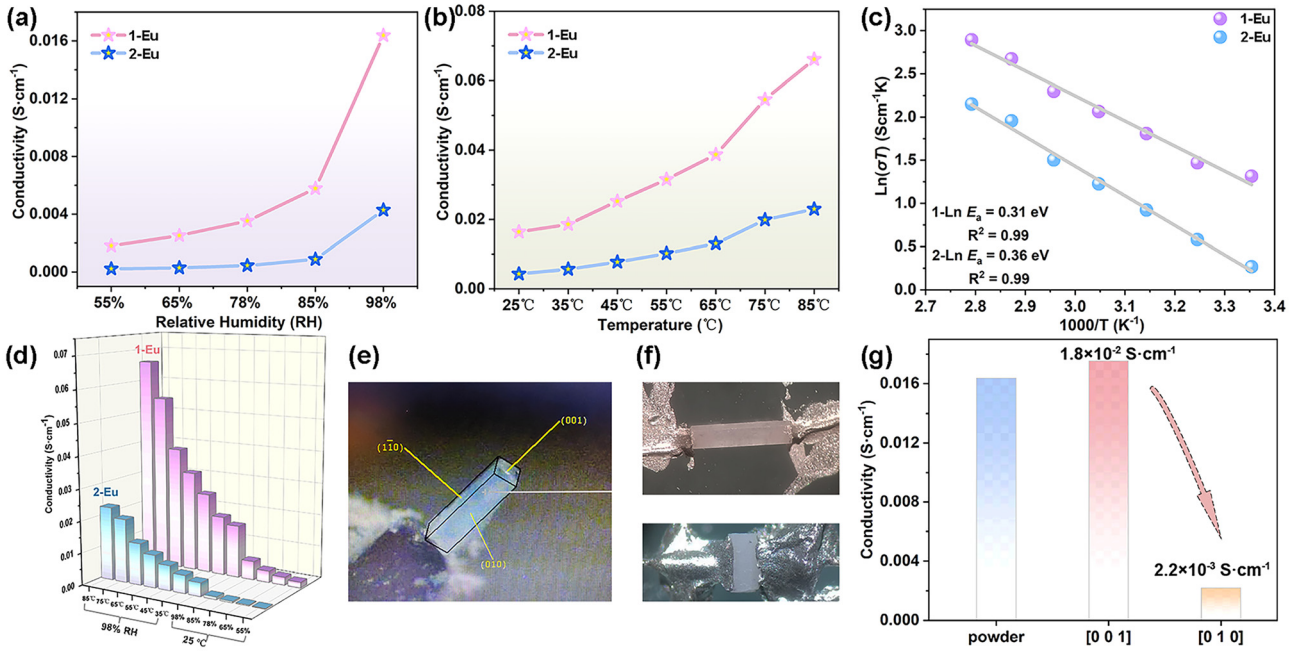

Fig. 3 (a and b) The broken-line graphs of proton conductivity of **1-Eu** and **2-Eu** under different relative humidity levels at 25 °C (a) and at different temperatures under 98% RH (b); (c) Arrhenius plots of the proton conductivities of **1-Eu** and **2-Eu**; (d) comparison graph of the proton conductivities of **1-Eu** and **2-Eu**; (e) orientation index of the single-crystal of **1-Eu**; (f) photographs of the single-crystal of **1-Eu** for proton conductivity along the [001] direction and the [010] direction. (g) comparison graph of the proton conductivity of pellet and singe-crystal samples along the [001] and [010] direction at 98% RH and 25 °C.

increase in humidity. This indicates that the adsorption of free water molecules within the framework could enhance the proton conductivity of **1-Eu** and **2-Eu** by improving the continuity and flexibility of the hydrogen bonding networks.

The temperature-dependent proton conductivities of **1-Eu** and **2-Eu** were further examined over a temperature range of 25–85 °C at 98% RH (Table S3†). The proton conductivity values of both compounds increase with increasing temperature. The conductivities reach their maximum value of 6.6×10^{-2} S cm^{-1} for **1-Eu** and 2.3×10^{-2} S cm^{-1} for **2-Eu**, respectively at 98% RH and 85 °C. These values are significantly higher than those of most other POMs reported in the literature (Table S4†). Notably, **1-Eu** exhibits one of the highest proton conductivities among POM-based materials, regardless of the conditions – whether at low temperature and low humidity (25 °C, 55% RH) or high temperature and high humidity (85 °C, 98% RH). The enhanced proton mobility at elevated temperatures arises from accelerated reorientation kinetics of the proton carriers compared to lower temperature conditions. Linear fitting of the temperature-dependent Arrhenius equation ($\sigma_T = \sigma_0 \exp(-E_a/k_bT)$) reveals an activation energy E_a of 0.31 eV for **1-Eu** and 0.36 eV for **2-Eu** under 98% RH (Fig. 3b, 3c and Fig. S10b, S10d†). These E_a values align with the characteristic range (0.1–0.4 eV) for proton conduction *via* the Grotthus mechanism wherein proton conduction occurs through a proton hopping over the hydrogen-bonded networks. This phenomenon is facilitated by the abundant proton carriers in **1-Eu** and **2-Eu** frameworks, including water molecules, terminal oxygen atoms of POTs and N-containing ligands, which facilitate the formation of hydrogen bond proton "hopping" networks.

The structure of **1-Eu** features a continuous, robust and dense hydrogen-bonding network formed by free water molecules and terminal oxygen atoms of the POMs within the hexagonal channels. This extensive network enables efficient proton transfer, thereby endowing **1-Eu** with high proton conductivity. In contrast, **2-Eu** adopts a two-dimensional layered structure with the water molecules and MePIP molecules intercalated between the layers. Although hydrogen bonds are present among the water molecules, the terminal oxygen atoms of POMs and the uncoordinated amino groups of MePIP, the hydrophobic methyl groups of MePIP are exposed on the periphery of POM clusters of **2-Eu**. This arrangement restricts the continuity of the hydrogen-bonding network, thereby potentially impeding proton conduction. As a result, **1-Eu** exhibits higher proton conductivities than **2-Eu** under identical test conditions (Fig. 2c and f).

The structural features of the hydrophilic 1D nanochannels in **1-Eu** prompt us to investigate the anisotropic proton conductivities along the specific crystallographic directions to further elucidate the relationship between the crystal structure and proton conductivities.

Fortunately, an ideal columnar single crystal of **1-Eu** was oriented with a Bruker Apex-II CCDdetector diffractometer, with the crystal faces indexed to [001], [010] and [1$\bar{1}$0] (Fig. 3e and Fig. S11†). AC impedance spectroscopy measurements were performed on the single crystal of **1-Eu** along the [001] channel

direction and the [010] direction perpendicular to the channel (Fig. 3f). As shown in Fig. 3g, at 98% RH and 25 °C, the pronton conductivity of **1-Eu** along the channel direction is 1.8×10^{-2} S cm^{-1}, approximately 8 times higher than that along the [010] direction (2.2×10^{-3} S cm^{-1}). Notably, the conductivity along the channel direction in the single-crystal sample exceeds that (1.6×10^{-2} S cm^{-1}) measured on the compressed pellet samples under the same conditions. These observations indicate that proton conduction in **1-Eu** is highly anisotropic, with the primary conducting pathway aligned along the 1D nanochannels. To our knowledge, only a few examples of POM-based single-crystal proton conductors have been reported in the literature (Table S5†). The single-crystal proton conductivity of **1-Eu** is comparable to those of various MOF materials, highlighting its potential as a high-performance proton conductor. The relatively high proton conductivity along the single-crystal *c*-axis direction could be attributed to the O-rich POM anions and abundant guest water molecules confined within the hydrophilic 1D hexagonal nanotubes as well as the coordinated water molecules. These fragments form extensive hydrogen-bonding interactions, creating a fast and efficient proton-transport pathway along the channel direction.

Luminescence properties

POMs serve as highly efficient luminescent sensitizers by capturing light and transferring energy to the excited states of the Ln^{III} ions, thereby significantly enhancing the emission intensity of the Ln centers. This unique capability enables Ln-based POM materials to achieve multi-color emission, making them highly promising candidates for applications in white LEDs, lighting, and displays. We have synthesized two series of POM-ligated Ln_{21}-clusters, namely **1-Ln** (Ln = Eu, Gd, Tb, Dy) and **2-Ln**(Ln = Eu, Tb), and systematically investigated their multi-color emission properties. The luminescence properties of **1-Ln** and **2-Ln** were found to be similar (Fig. 4 and Fig. S12, S13†), thus we focused on the detailed study of **1-Ln** (Fig. 4a). Upon excitation at 395 nm, the fluorescence spectrum of **1-Eu** in the solid state at room temperature exhibits intense red luminescence bands at 580 nm, 595 nm, 618 nm, 652 nm and 701 nm. These emissions correspond to the $^5D_0 \rightarrow {}^7F_J$ (J = 0, 1, 2, 3, 4) transition of the Eu^{3+} ion. The strongest emission peak at 618 nm of **1-Eu** is attributed to the $^5D_0 \rightarrow {}^7F_2$ electronic transition, which confirms the absence of inversion symmetry at the Eu^{3+} site. This is consistent with the structural analysis. The observed magnetic dipole transition at 598 nm ($^5D_0 \rightarrow {}^7F_1$) further corroborates the local coordination environment. Furthermore, The Commission Internationale de L'Eclairage (CIE) chromaticity coordinates of **1-Eu** were determined to be (0.667, 0.331) (Fig. 4b). Moreover, the luminescence decay curve of **1-Eu** was also obtained and fitted well by a single exponential function as $I = A\exp(-t/\tau)$ with a luminescence lifetime τ of 768 μs (Fig. S12c†).

The luminescence intensity of Ln-based materials is generally highly dependent on the ambient temperature due to non-radiative relaxation, energy transfer, or crossover processes. As shown in Fig. 4d, the temperature-dependent luminescence spectra of **1-Eu** were measured at varying temperatures ranging

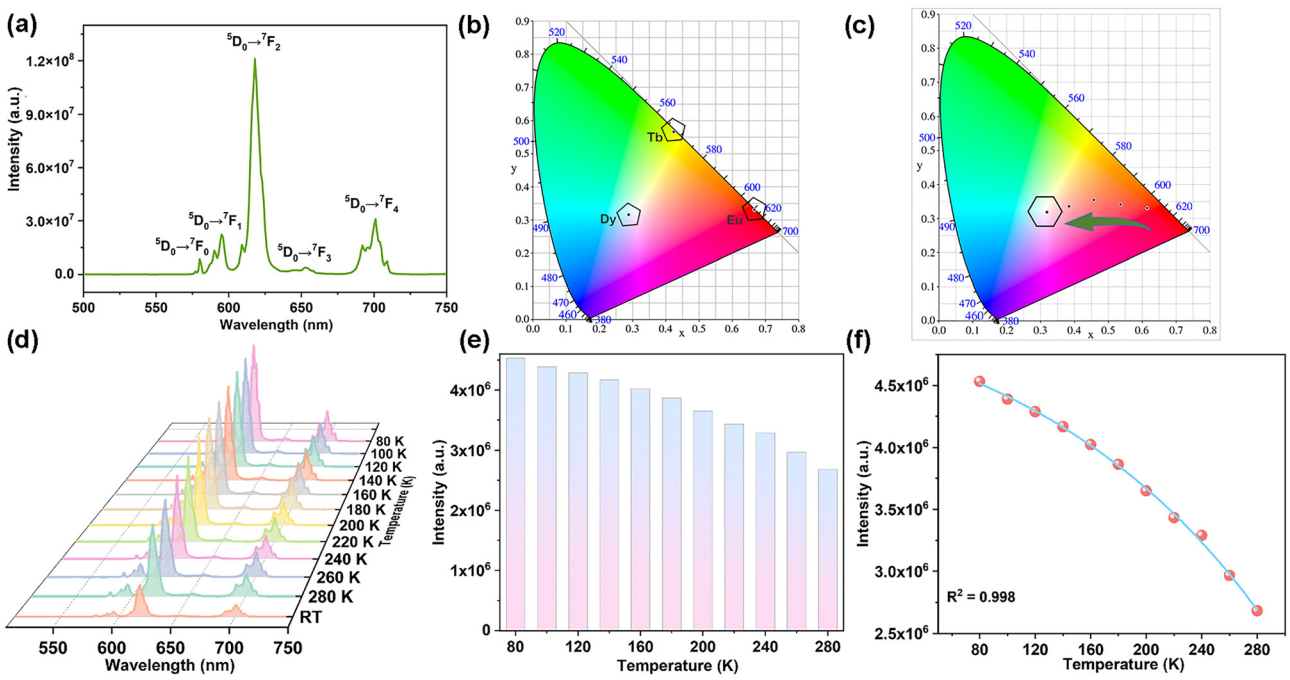

Fig. 4 (a) Room-temperature solid-state emission spectrum of **1-Eu**; (b) and (c) CIE coordinates for **1-Eu**, **1-Tb**, **1-Dy** and **1-Eu$_x$Dy$_{1-x}$** with $0 \le x \le 1$; (d) temperature-dependent solid-state emission spectra of **1-Eu**; (e) intensities of the major characteristic peaks of **1-Eu** at 618 nm at different temperatures; (f) exponential fitting of the intensity data in the 80 to 280 K range of **1-Eu** at 618 nm.

from 80 to 298 K. As the temperature increases from 80 K to 298 K, the intensity of all transitions decreases at an average rate of 0.2% per Kelvin, with an intensity ratio of $I_{80\ K}/I_{298\ K}$ of about 1.8 for the $^5D_0 \rightarrow {}^7F_2$ transition (618 nm). This phenomenon can be attributed to the presence of thermally activated non-radiative relaxation pathways, including phonon-assisted energy transfer and ligand-to-metal charge transfer (LMCT) state destabilization. This trend is associated with a general decrease in line height, but no significant shift in peak position, indicating the absence of major structural changes with temperature. The temperature-dependent luminescence intensity of **1-Eu** can be fitted by the following equation $I = -5.5 \times 10^5 \exp(T/176.9) + 5.4 \times 10^6$ ($R^2 = 0.998$) (Fig. 4e and 4f). This model provides insights into the thermal quenching mechanisms observed in europium-based materials.

In the solid state, upon excitation at 352 nm, **1-Dy** exhibits light blue luminescence with three characteristic emission peaks for the Dy^{3+} ion at 480, 573, and 663 nm and has CIE coordinates of (0.288, 0.317) (Fig. 4b and Fig. S12a†). These peaks correspond to the $^4F_9 \rightarrow {}^6H_J$ transitions of the Dy^{3+} ion (J = 15/2, 13/2, and 11/2). Upon excitation at 485 nm, **1-Tb** emits intense yellow-green luminescence with CIE coordinates of (0.424, 0.567), displaying a typical Tb^{3+} emission spectrum. The emission peaks at 545, 587, and 622 nm arise from the transitions of Tb^{3+} ions from the $^5D_4$ excited state to the ground state ^7F_J (J = 6, 5, 4, 3) of the Tb^{3+} ions (Fig. 4b and Fig. S12b†).

Given the isostructural frameworks of **1-Eu** and **1-Dy**, an efficient strategy was developed to generate white luminescence by doping different ratios of Eu^{3+} ions in **1-Dy** and modulating the Ln^{3+} ratio. By changing the ratios of Eu^{3+} and Dy^{3+}, as confirmed by ICP, the structures **1-Eu$_x$Dy$_{1-x}$** (x = 0.25, 0.40, 0.60, 0.75, 0.85, 1) are not significantly changed, as confirmed by comparing the IR spectra and crystal cell parameters with that of **1-Ln** (Tables S6–S8 and Fig. S14†). The unique Eu/Dy-doped **1-Eu$_x$Dy$_{1-x}$** samples exhibit dual emissions from Eu^{3+} and Dy^{3+} ions upon excitation at 395 nm in the solid state. As shown in Fig. 4c, the **1-Eu$_x$Dy$_{1-x}$** samples display different light emissive colors corresponding to different ratios of the Eu^{3+} and Dy^{3+} ions (x = 0.25, 0.40, 0.60, 0.75, 0.85, 1). The corresponding luminescence color coordinates are summarized in Table S9.† Notably, the calculated chromaticity coordinates for **1-Eu$_{0.25}$Dy$_{0.75}$**, with CIE coordinates of (0.32, 0.32) are very close to the standard white light (0.333, 0.333) according to the 1931 Commission Internationale de L'Eclairage (CIE) chromaticity diagram. Consequently, the combination of light blue (Dy^{3+}) and red (Eu^{3+}) emissions generates white light emission, leading to a novel single-phased white-light emitting material.

Conclusions

In summary, two series of giant high-nuclearity {**Eu$_{27}$Se$_{10}$Ge$_9$W$_{91}$**}-containing tungstogermanates, namely, **1-Ln** and **2-Ln**, have been successfully synthesized under alkaline conditions, employing Na_2SeO_3 as the anionic template and organic amines as basic ligands, respectively. The {$Eu_{27}Se_{10}Ge_9W_{91}$}-1 or {$Eu_{27}Se_{10}Ge_9W_{91}$}-2 cluster exhibits a unique windwheel-shaped Ln_{21}-oxo-cluster-embedded, three-layered sandwich structure. Notably, the giant windmill-shaped Eu_{21}-cluster has been reported for the first time. **1-Ln** features a 3D inorganic framework with 1D nanochannels based on 5-connected *bnn* net, whereas **2-Ln** presents a 2D inorganic–organic layered network. Notably, compounds **1-Eu** and **2-Eu** display distinct proton conduction properties due to their different packing structures. In particular, **1-Eu** demonstrates high single-crystal proton conductivity along its 1D channels in **1-Eu**. Additionally, **1-Eu** exhibits temperature-dependent fluorescence. The emission colors can be fine-tuned by adjusting the ratio of lanthanide ions. Furthermore, co-doping with Eu^{3+} and Dy^{3+} ions enables the adjustment of emission color and the achievement of white light emission. This work introduces a series of bifunctional Ln-POTs with high single-crystal proton conductivity and tunable luminescence, offering valuable insights for the development of versatile switchable materials based on high-nuclearity Ln-POTs.

Author contributions

Yun-Fei Cao: investigation, data curation, major experiments, writing – original draft and editing, and writing – review and editing. Xin-Rong Jin: formula analysis, software, and data curation. Wen-Jun Xia: investigation and data curation. Yan-Qiong Sun: writing – review and editing, project administration, and funding acquisition. Xin-Xiong Li: software, funding acquisition, and conceptualization. Shou-Tian Zheng: project administration, funding acquisition, and conceptualization.

Conflicts of interest

There are no conflicts to declare.

Data availability

All the data in this study are provided in the main text and the ESI.† Crystallographic data for the structures reported have been deposited at the Cambridge Crystallographic Data Center with CCDC reference numbers 2387252 and 2387262† for compounds **1-Eu** and **2-Eu**, respectively.

Acknowledgements

We gratefully acknowledge the financial support from the Natural Science Fund of Fujian Province (No. 2024J01234) and the National Natural Science Foundation of China (No. 21971040, 22371046 and 22171045).

References

1 Y. Liu, H. Li, C. Lu, P. Gong, X. Ma, L. Chen and J. Zhao, Organocounterions-Assisted and pH-Controlled Self-Assembly of Five Nanoscale High-Nuclear Lanthanide Substituted Heteropolytungstates, *Cryst. Growth Des.*, 2017, **17**, 3917–3928.

2 P. Ma, R. Wan, Y. Wang, F. Hu, D. Zhang, J. Niu and J. Wang, Coordination-Driven Self-Assembly of a 2D Graphite-Like Framework Constructed from High-Nuclear Ce10 Cluster Encapsulated Polyoxotungstates, *Inorg. Chem.*, 2016, **55**, 918–924.

3 P. Yang, M. Alsufyani, A. H. Emwas, C. Chen and N. M. Khashab, Lewis Acid Guests in a $\{P_8W_{48}\}$ Archetypal Polyoxotungstate Host: Enhanced Proton Conductivity via Metal–Oxo Cluster within Cluster Assemblies, *Angew. Chem., Int. Ed.*, 2018, **57**, 13046–13051.

4 Y.-N. Gu, D. Zhao, H. Yu, R. Ge, Z. Li, C.-B. Tian, X.-X. Li, Y.-Q. Sun and S.-T. Zheng, Incorporating polyoxometalates and organic ligands to pursue 3d–4f heterometallic clusters: a series of $\{Cr_4Ln_4\}$ clusters stabilized by phthalic acid and $[SiW_{12}O_{40}]^{4-}$, *RSC Adv.*, 2019, **9**, 13543–13549.

5 Y. Hao, L. Zhong, H.-H. Li and S.-T. Zheng, Two Lanthanide-Substituted Polyoxometalates Featuring Novel Crescent-Shaped Ln5 Clusters: Structures, Ion Conductivities, and Magnetic Properties, *Cryst. Growth Des.*, 2019, **19**, 1329–1335.

6 H.-Y. Wang, S.-R. Li, X. Wang, L.-S. Long, X.-J. Kong and L.-S. Zheng, Enhanced proton conductivity of Mo_{154}-based porous inorganic framework, *Sci. China: Chem.*, 2021, **64**, 959–963.

7 Q.-S. Lai, X.-X. Li and S.-T. Zheng, All-inorganic POM cages and their assembly: A review, *Coord. Chem. Rev.*, 2023, **482**, 215077–215094.

8 S.-Y. Liu, X.-X. Li, W.-C. Chen, K.-Z. Shao, X.-L. Wang, C. Qin and Z.-M. Su, A highly reduced Mo_{74} polyoxometalate featuring high proton conductivity accessed by building block strategy, *Sci. China: Chem.*, 2023, **67**, 862–868.

9 Y.-M. Cui, Y.-J. Zhu, J. Sun, D. Wu, X. Wang, X.-S. Wu and Z.-M. Su, Swift Proton Release Enhancing Proton Conductivity in Anderson-Polyoxometalates-Based Metal–Organic Frameworks, *ACS Mater. Lett.*, 2024, **6**, 4255–4261.

10 L. Jia, Y.-X. Liu, X.-X. Li, C. Sun and S.-T. Zheng, A Palladium-Containing Polyoxotungstate with Anisotropic Proton Conductivity, *Inorg. Chem.*, 2024, **63**, 14308–14312.

11 Y. Sun, Y. Zou, H. Li, W. Chen, P. Ma, J. Niu and J. Wang, Controlled Assembly of a Dawson-like Antimoniotungstate-Supported Trefoil-type Trimer with Good Proton Conductivity Performance, *Inorg. Chem.*, 2024, **63**, 2363–2369.

12 N. Ogiwara, T. Iwano, T. Ito and S. Uchida, Proton conduction in ionic crystals based on polyoxometalates, *Coord. Chem. Rev.*, 2022, **462**, 214524–214537.

13 R.-L. Liu, Y. Chen, X. Su, W. Zhu, Z. Liu, Y. Chen, D.-Y. Wang and G. Li, Proton conductive polyoxometalates, *Coord. Chem. Rev.*, 2025, **522**, 216224–216254.

14 S. An, J.-C. Liu, H. Zhang, L. Wu, B. Qi and Y.-F. Song, Recent progress on the frontiers of polyoxometalates structures and applications, *Sci. China: Chem.*, 2018, **62**, 159–161.

15 D. Wang, J. Jiang, M.-Y. Cao, S.-S. Xie, Y.-M. Li, L.-J. Chen, J.-W. Zhao and G.-Y. Yang, An unprecedented dumbbell-shaped pentadeca-nuclear W-Er heterometal cluster stabilizing nanoscale hexameric arsenotungstate aggregate and electrochemical sensing properties of its conductive hybrid film-modified electrode, *Nano Res.*, 2021, **15**, 3628–3637.

16 L. Zhang, P. Li, A. Zhao, X. Li, J. Tang, F. Zhang, G. Jia and C. Zhang, Synthesis, structure, and color-tunable luminescence properties of lanthanide activator ions doped bismuth silicate as single-phase white light emitting phosphors, *J. Alloys Compd.*, 2020, **816**, 152546–152555.

17 B. Zhang, J. Zhang, Y. Guo, J. Wang, J. Xie, X. Li, W. Huang, L. Wang and Q. Zhang, Synthesis and photoluminescence of double perovskite La_2LiSbO_6:Ln^{3+} (Ln= Eu, Tb, Tm, Sm, Ho) phosphors and enhanced luminescence of La_2LiSbO_6:Eu^{3+} red phosphor via Bi^{3+} doping for white light emitting diodes, *J. Alloys Compd.*, 2019, **787**, 1163–1172.

18 K. Li, M. Shang, H. Lian and J. Lin, Recent development in phosphors with different emitting colors via energy transfer, *J. Mater. Chem. C*, 2016, **4**, 5507–5530.

19 C.-H. Huang, W.-R. Liu, T.-S. Chan and Y.-T. Lai, Orangish-yellow-emitting $Ca_3Si_2O_7$:Eu^{2+} phosphor for application in blue-light based warm-white LEDs, *Dalton Trans.*, 2014, **43**, 7917–7923.

20 C.-H. Huang, D.-Y. Wang, Y.-C. Chiu, Y.-T. Yeh and T.-M. Chen, $Sr_8MgGd(PO_4)_7$:Eu^{2+}: yellow-emitting phosphor for application in near-ultraviolet-emitting diode based white-light LEDs, *RSC Adv.*, 2012, **2**, 9130–9134.

21 C. M. Granadeiro, D. Julião, S. O. Ribeiro, L. Cunha-Silva and S. S. Balula, Recent advances in lanthanide-coordinated polyoxometalates: from structural overview to functional materials, *Coord. Chem. Rev.*, 2023, **476**, 214914–214935.

22 W.-J. Xia, Y.-J. Wang, Y.-F. Cao, C. Sun, X.-X. Li, Y.-Q. Sun and S.-T. Zheng, A luminescent folded S-shaped high-nuclearity Eu19-oxo-cluster embedded polyoxoniobate for information encryption, *Chin. Chem. Lett.*, 2025, **36**, 110248–110252.

23 D. Wang, Y. Li, Y. Zhang, X. Xu, Y. Liu, L. Chen and J. Zhao, Construction of Ln^{3+}-Substituted Arsenotungstates Modified by 2,5-Thiophenedicarboxylic Acid and Application in Selective Fluorescence Detection of Ba^{2+} in Aqueous Solution, *Inorg. Chem.*, 2020, **59**, 6839–6848.

24 S. Wang, T. Gong, L. Chen and J. Zhao, Pyrazine Dicarboxylic Acid and Phosphite-Bridging Lanthanide-Incorporated Tellurotungstates and Their Fluorescence Performances, *Inorg. Chem.*, 2024, **63**, 20470–20481.

25 H. Wu, M. Zhi, V. Singh, H. Li, P. Ma, J. Niu and J. Wang, Elucidating white light emissions in Tm^{3+}/Dy^{3+} codoped polyoxometalates: a color tuning and energy transfer mechanism study, *Dalton Trans.*, 2018, **47**, 13949–13956.

26 Y.-J. Wang, S.-Y. Wu, Y.-Q. Sun, X.-X. Li and S.-T. Zheng, Octahedron-shaped three-shell Ln_{14}-substituted polyoxotungstogermanates encapsulating a W_4O_{15} cluster: lumine-

scence and frequency dependent magnetic properties, *Chem. Commun.*, 2019, **55**, 2857–2860.

27 B. S. Bassil, M. H. Dickman, I. Römer, B. von der Kammer and U. Kortz, The Tungstogermanate $[Ce_{20}Ge_{10}W_{100}O_{376}(OH)_4(H_2O)_{30}]^{56-}$: A Polyoxometalate Containing 20 Cerium(III) Atoms, *Angew. Chem., Int. Ed.*, 2007, **46**, 6192–6195.

28 S. Reinoso, M. Giménez-Marqués, J. R. Galán-Mascarós, P. Vitoria and J. M. Gutiérrez-Zorrilla, Giant Crown-Shaped Polytungstate Formed by Self-Assembly of CeIII–Stabilized Dilacunary Keggin Fragments, *Angew. Chem., Int. Ed.*, 2010, **49**, 8384–8388.

29 Z. Li, X. X. Li, T. Yang, Z. W. Cai and S. T. Zheng, Four–Shell Polyoxometalates Featuring High–Nuclearity Ln_{26} Clusters: Structural Transformations of Nanoclusters into Frameworks Triggered by Transition–Metal Ions, *Angew. Chem., Int. Ed.*, 2017, **56**, 2664–2669.

30 Z. Li, Z.-H. Lv, H. Yu, Y.-Q. Sun, X.-X. Li and S.-T. Zheng, Giant Ln_{30}-Cluster-Embedded Polyoxotungstate Nanoclusters with Exceptional Proton-Conducting and Luminescent Properties, *CCS Chem.*, 2022, **4**, 2938–2945.

31 M.-Y. Yao, Y.-F. Liu, X.-X. Li, G.-P. Yang and S.-T. Zheng, The largest Se-4f cluster incorporated polyoxometalate with high Lewis acid–base catalytic activity, *Chem. Commun.*, 2022, **58**, 5737–5740.

32 L. Liu, J. Jiang, G. Liu, X. Jia, J. Zhao, L. Chen and P. Yang, Hexameric to Trimeric Lanthanide-Included Selenotungstates and Their 2D Honeycomb Organic–Inorganic Hybrid Films Used for Detecting Ochratoxin A, *ACS Appl. Mater. Interfaces*, 2021, **13**, 35997–36010.

33 Q. Han, Z. Li, X. Liang, Y. Ding and S.-T. Zheng, Synthesis of a 6-nm-Long Transition-Metal–Rare-Earth-Containing Polyoxo metalate, *Inorg. Chem.*, 2019, **58**, 12534–12537.

34 W.-C. Chen, C.-Q. Jiao, X.-L. Wang, K.-Z. Shao and Z.-M. Su, Self-Assembly of Nanoscale Lanthanoid-Containing Selenotungstates: Synthesis, Structures, and Magnetic Studies, *Inorg. Chem.*, 2019, **58**, 12895–12904.

35 K. Wassermann, M. H. Dickman and M. T. Pope, Self–Assembly of Supramolecular Polyoxometalates: The Compact, Water–Soluble Heteropolytungstate Anion $[AsCe(H_2O)_{36}W_{148}O_{524}]^{76-}$, *Angew. Chem., Int. Ed.*, 2003, **36**, 1445–1448.

36 F. Hussain and G. R. Patzke, Self-assembly of dilacunary building blocks into high-nuclear $[Ln_{16}As_{16}W_{164}O_{576}(OH)_8(H_2O)_{42}]^{80-}$(Ln = EuIII, GdIII, TbIII, DyIII, and HoIII) polyoxotungstates, *CrystEngComm*, 2011, **13**, 530–536.

37 J. C. Liu, J. F. Wang, Q. Han, P. Shangguan, L. L. Liu, L. J. Chen, J. W. Zhao, C. Streb and Y. F. Song, Multicomponent Self–Assembly of a Giant Heterometallic Polyoxotungstate Supercluster with Antitumor Activity, *Angew. Chem., Int. Ed.*, 2021, **60**, 11153–11157.

38 N. Song, M. Lu, J. Liu, M. Lin, P. Shangguan, J. Wang, B. Shi and J. Zhao, A Giant Heterometallic Polyoxometalate Nanocluster for Enhanced Brain–Targeted Glioma Therapy, *Angew. Chem., Int. Ed.*, 2024, **63**, e202319700–e202319707.

39 J. C. Liu, Q. Han, L. J. Chen, J. W. Zhao, C. Streb and Y. F. Song, Aggregation of Giant Cerium–Bismuth Tungstate Clusters into a 3D Porous Framework with High Proton Conductivity, *Angew. Chem., Int. Ed.*, 2018, **57**, 8416–8420.

40 J.-H. Liu, R.-T. Zhang, J. Zhang, D. Zhao, X.-X. Li, Y.-Q. Sun and S.-T. Zheng, A Series of 3D Porous Lanthanide-Substituted Polyoxometalate Frameworks Based on Rare Hexadecahedral $\{Ln_6W_8O_{28}\}$ Heterometallic Cage-Shaped Clusters, *Inorg. Chem.*, 2019, **58**, 14734–14740.

41 L. Yu, J. Ye, D.-H. Li, Y.-Q. Sun, X.-X. Li and S.-T. Zheng, A tetrahedron-shaped polyoxoantimotungstate encapsulating a hexanuclear octahedral lanthanide-oxo cluster for an amperometric bromate sensor, *Dalton Trans.*, 2024, **53**, 5258–5265.

42 C. Liu, S. Zhang, Y. Dai, F. Wu, J. Liu and J. Zhao, Multinuclear Antimony–Bismuth–Lanthanide Cluster-Connected Polyoxometalate for the Detection of 5-Hydroxyindoleacetic Acid via Luminescence, *Inorg. Chem.*, 2024, **63**, 24825–24833.

43 H.-P. Xiao, R.-T. Zhang, Z. Li, Y.-F. Xie, M. Wang, Y.-D. Ye, C. Sun, Y.-Q. Sun, X.-X. Li and S.-T. Zheng, Organoamine-Directed Assembly of 5p–4f Heterometallic Cluster Substituted Polyoxometalates: Luminescence and Proton Conduction Properties, *Inorg. Chem.*, 2021, **60**, 13718–13726.

44 Z. Li, L. D. Lin, D. Zhao, Y. Q. Sun and S. T. Zheng, A Series of Unprecedented Linear Mixed–Metal–Substituted Polyoxometalate Trimers: Syntheses, Structures, Luminescence, and Proton Conductivity Properties, *Eur. J. Inorg. Chem.*, 2018, **2019**, 437–441.